Aging and Disease
www.aginganddisease.org
Early access date: November 9, 2026
http://dx.doi.org/10.14336/AD.2026.0944

Original Article

Targeting Mitochondrial MAVS Signaling in Deep-Senescent Hematopoietic Stem Cells Ameliorates Infection-Driven Immunosenescence

Weinian Liao[1#], Yue Zhang[1#], Yetong Wang[1#], Ruzhou Zhao[1#], Cheng Xu[1,2], Tianyue Wang[1], Mingyang Xie[1], Zhang Zhang[1], Xiaodong Zai[1], Zhongyi Wang[1], Jun Zhang[1*], Junjie Xu[1*]

[1]National Key Laboratory of Advanced Biotechnology, Academy of Military Medical Sciences, Beijing, China.
[2]Department of Hepatobiliary Surgery, Mianyang 404 Hospital, Mianyang, Sichuan, China.

[Received July 15, 2026; Revised November 3, 2026; Accepted November 5, 2026]

ABSTRACT: Acute viral infections cause immediate tissue damage and exert long-term detrimental effects on host immunity and hematopoiesis. However, the mechanisms by which infection drives hematopoietic stem cell (HSC) aging and accelerates immunosenescence remain poorly defined. Here, using a non-lethal influenza A virus (IAV) infection model, we demonstrate that middle-aged mice, rather than young mice, are uniquely susceptible to infection-driven immune deterioration. Infection superimposed on baseline physiological aging drives sustained chronic inflammation and accelerated immunosenescence in middle-aged mice. We identify an infection-induced deep senescence state of HSCs as a major contributor to systemic immunosenescence. This deep senescence state is characterized by p16 upregulation, elevated aging markers, increased my-HSC frequency, and mitochondrial dysfunction. Mechanistically, disrupted mitochondrial homeostasis triggers cytosolic mitochondrial RNA (mtRNA) accumulation and sustained MAVS pathway activation, forming a pathogenic feedforward loop that perpetuates HSC aging. Through high-throughput screening, we identify Bilobetin, a natural biflavonoid, as a potent mitochondria-targeted compound that restores mitochondrial fitness, dampens aberrant MAVS signaling, and ameliorates both HSC aging and systemic immunosenescence. Collectively, our findings establish a hematopoietic-immune senescence stratification model and delineate the molecular threshold separating physiological adaptation from pathological deterioration in infection-driven aging, identifying mitochondria-targeted interventions as a therapeutic strategy for mitigating infection-induced immuno-senescence.

Key words: Immunosenescence, Hematopoietic stem cell, Viral infection, MAVS signaling, Senescence

INTRODUCTION

Acute viral infections inflict immediate tissue damage and exert long-term deleterious effects on host immunity and hematopoiesis. Beyond acute pathogenicity, accumulating clinical and experimental evidence demonstrates that viral clearance often fails to fully restore immune homeostasis, leading to persistent low-grade inflammation, impaired immune function, and accelerated aging phenotypes [1-4]. These long-term sequelae exhibit striking age-dependent heterogeneity: young individuals generally achieve complete immune recovery, whereas middle-aged and older populations suffer from prolonged immune dysfunction and elevated risk of age-related disorders post-infection [2, 5]. Nevertheless, the cellular and molecular mechanisms underlying this age-dependent divergence in infection-driven immune deterioration remain largely uncharacterized, and the critical threshold separating physiological adaptive responses from pathological aging progression has yet to be defined.

Cellular senescence, classically marked by *Cdkn2a* (encoding p16) upregulation and stable cell cycle arrest, acts as a context-dependent double-edged process. Transient senescence induction serves as a physiological homeostatic mechanism that supports tissue repair, limits fibrosis, and regulates embryonic development [6, 7].

***Correspondence should be addressed to:** Junjie Xu (Email: xujunjie@sina.com) or Jun Zhang (Email: justforhere@126.com), National Key Laboratory of Advanced Biotechnology, Academy of Military Medical Sciences, Beijing, 100071, China. [#]These authors contributed equally to this work.

Copyright: © 2026 Liao W. et al. This is an open-access article distributed under the terms of the Creative Commons Attribution License, which permits unrestricted use, distribution, and reproduction in any medium, provided the original author and source are credited.

Similarly, the senescence-associated secretory phenotype (SASP) exerts context-dependent functions: transient, moderate SASP promotes immune surveillance and tissue regeneration, while chronic, unresolved SASP drives sterile inflammation and progressive tissue dysfunction [8]. Viral infection and cellular stress further expand the pool of p16-high senescent cells across immune and stromal compartments, reshaping host immune responsiveness and tissue integrity [9, 10]. However, most existing studies treat senescent cells as a homogeneous population, failing to resolve the distinct senescence burden and functional heterogeneity across peripheral immune cells and bone marrow (BM) hematopoietic stem cells (HSCs) [11, 12]. It also remains unclear how infection-induced senescence transitions from a transient adaptive state to a persistent pathological state.

As the clonal origin of all hematopoietic and immune lineages, HSCs play a central role in maintaining lifelong immune homeostasis and resilience. Compared with young counterparts, middle-aged mice already exhibit canonical hallmarks of physiological HSC aging, including numeric expansion, myeloid-biased differentiation, impaired self-renewal capacity, epigenetic drift, elevated reactive oxygen species (ROS), and compromised mitochondrial fitness [13-15]. This pre-existing baseline aging landscape likely renders middle-aged individuals uniquely vulnerable to infection-induced hematopoietic deterioration. In line with this notion, aged adults recovering from severe viral infections frequently present with prolonged fatigue and sustained immune dysregulation, hallmarks collectively indicative of accelerated biological aging [2, 5]. Despite these clinical observations, a direct causal link between acute viral infection and accelerated HSC aging remains unestablished, and the upstream molecular drivers of infection-induced HSC aging are poorly understood.

In this study, we employ a non-lethal influenza A virus (IAV) infection model in young (2-month-old) and middle-aged (12-month-old) mice to dissect age-dependent virus-host interactions governing infection-driven immune and HSC aging. We demonstrate that middle age represents a distinct susceptibility window for infection-driven immune deterioration and identify a deep senescence state in HSCs as a major contributor to systemic immunosenescence. Mechanistically, we reveal that disrupted mitochondrial homeostasis drives cytosolic mitochondrial RNA (mtRNA) accumulation and sustained MAVS pathway activation, forming a pathogenic feedforward loop that perpetuates HSC aging. Through high-throughput screening, we identify Bilobetin, a natural biflavonoid, as a potent mitochondria-targeted compound that restores mitochondrial fitness and ameliorates both HSC aging and systemic immunosenescence. Collectively, our findings establish a hematopoietic-immune senescence stratification model and delineate the molecular threshold separating physiological adaptation from pathological deterioration in infection-driven aging, providing promising mitochondria-targeted strategies for mitigating infection-induced immunosenescence.

MATERIALS AND METHODS

Animals

Wild-type (WT) C57BL/6 mice, including young (2-month-old) and middle-aged (12-month-old) experimental cohorts, were obtained from HFK Bioscience Co., Ltd. (Beijing, China) and SPF Biotechnology Co., Ltd. (Beijing, China). Multiple transgenic mouse lines on a congenic C57BL/6 background were acquired from validated commercial sources as follows: B6.Cg-Tg(Mx1-cre)1Cgn/J (*Mx1-Cre*) lines were sourced from The Jackson Laboratory (Bar Harbor, ME, USA); C57BL/6NCya-*Mavs*^{em1flox}/Cya (*Mavs*$^{f/f}$) mice were procured from Cyagen Biosciences (Guangzhou, China). To generate *Mx1-Cre*-mediated inducible *Mavs* conditional knockout (KO) mice, *Mavs*$^{f/f}$ mice were interbred with *Mx1-Cre* transgenic mice. *Mavs*$^{f/f}$*;Mx1-Cre* mice were administered Poly(I:C) (400 μg per mouse, intraperitoneally, every other day for 7 injections), and subsequent experiments were conducted 6 weeks after the first injection. Deletion efficiency in HSCs was confirmed by flow cytometry. For all *in vivo* assays involving the conditional knockout model, only male transgenic mice and age-matched *Mavs*$^{f/f}$ littermate controls were utilized. In conditional knockout experiments, the control groups received the same Poly(I:C) regimen as the conditional knockout mice (400 μg per mouse, intraperitoneally, every other day for 7 injections). All mice were background-matched, randomly allocated to experimental groups, and housed in strict specific pathogen-free (SPF) barrier facilities with ad libitum access to autoclaved rodent chow and sterile drinking water. All animal experimental protocols were reviewed and approved by the Institutional Animal Care and Use Committee (IACUC) of the Laboratory Animal Center (approval No. IACUC-DWZX-2025-025 and No. IACUC-SWGCYJS-2026-032), and all procedures were performed in strict compliance with institutional ethical guidelines for laboratory animal care and use.

Infection model

Mice were anesthetized with isoflurane and intranasally inoculated with H1N1 influenza virus A/Puerto Rico/8/34 (PR8; 100, 200 or 300 PFU), H1N1 influenza virus A/California/04/2009 (CA04; 4×10^2, 4×10^3 or 4×10^4

PFU), or mouse-adapted SARS-CoV-2 strain (MA10; 4×10^3 PFU) in 30 μL sterile PBS. Body weight and clinical scores were monitored daily. Clinical scores were assessed using a standardized scoring system [16] evaluating activity, posture, respiration, and appearance. Mice were euthanized at indicated time points for downstream analyses.

Preparation of mouse tissues

BM cells were isolated by pooling and crushing femurs and tibias in PBS (Sigma-Aldrich, St. Louis, MO, USA) supplemented with 2% fetal calf serum (FCS; Thermo Fisher Scientific, Carlsbad, CA, USA). Spleen was dissected and crushed in PBS with 2% FCS. Peripheral blood (PB) was collected from the tail veins of the mice. Lung and liver tissues were minced and digested in RPMI 1640 containing 1 mg/mL collagenase IV (Sigma-Aldrich) and 20 μg/mL DNase I (Sigma-Aldrich) for 45 min at 37°C with gentle agitation. Dissociated cells were passed through a 70-μm cell strainer, washed with PBS+2% FCS. Red blood cells (RBCs) were lysed using a red cell lysis buffer (StemCell Technologies, Vancouver, BC, Canada) for 5 min (15 min for spleen and PB) followed by washing and centrifugation for 5 min at 400×g. Subsequently, cells were filtered through a 40 μm cell strainer, and then analyzed or isolated by FACS as described below.

Flow cytometry and cell sorting

Prior to antibody staining, cells were Fc-blocked by incubation with 1 mg/mL rat IgG (Abcam) for 30 min on ice. Antibody staining was performed in Flow Cytometry Staining Buffer (eBioscience). Cells were incubated on ice for 30 min. For immunophenotypic analysis of HSCs gated as Lineage$^-$Sca-1$^+$c-Kit$^+$CD150$^+$Flt3$^-$CD48$^-$, BM cells were stained with a panel of fluorochrome-conjugated antibodies. For T cell phenotyping, cells were stained with CD3, CD8α, CD4, CD44, CD62L, and PD-1 antibodies. For B cell analysis, cells were surface-stained with CD43, CD21/CD35, IgM, CD19, IgD, CD93, CD23, and B220 antibodies. For intracellular ROS assessment, the DCFDA/H2DCFDA kit (Abcam) was used. Mitochondrial mass and membrane potential were measured using MitoTracker Green (MTG) and TMRE staining, respectively. For assessment of cytoplasmic protein expression, cells were stained with surface markers and carefully washed. Cells were fixed with IC Fixation buffer (eBioscience) at room temperature for 20 min and then permeabilized with Permeabilization buffer (eBioscience) in the presence of MAVS (Proteintech), IL-6 (BioLegend) or BIRC6 (Bioss) antibodies at room temperature for another 30 min and analyzed by flow cytometry. For assessment of nuclear protein expression, cells were fixed, permeabilized and stained using the Foxp3/Transcription Factor Staining Buffer Set (eBioscience) after surface staining. Subsequently, cells were stained with p16 (Bioss), p-IRF3 (Ser396) (Proteintech) and p-TBK1 (Ser172) (Proteintech) monoclonal antibodies. Cells were sorted using a FACSAria II (BD Biosciences) or analyzed on a Sony ID7000^{TM} spectral analyzer (Sony Biotechnology). All flow cytometry data were analyzed using FlowJo V10 software. For isolation of HSCs, BM cells were incubated in PBS+2% FCS for 20 min at 4°C with a Direct Lineage Cell Depletion Cocktail (Miltenyi Biotec, Bergisch Gladbach, Germany). Lineage-negative cells were enriched by magnetic separation. Antibodies used in Flow cytometry were detailed in Supplementary Table 1.

RNA-seq and bioinformatics analysis

Cells were sorted and total RNA was extracted using the RNeasy Micro Kit (QIAGEN). Libraries were prepared and sequenced on an Illumina NovaSeq 6000. Adaptors, undetermined bases, and low-quality bases were trimmed using Fastp. Reads were aligned, and gene expression was quantified using RSEM (v1.2.12). Differentially expressed genes (DEGs) were identified with DESeq2 (fold change >2.0, adjusted $P < 0.05$). Gene set enrichment analysis was performed using the Molecular Signatures Database (MSigDB, v6.0), and signaling pathways were analyzed with Ingenuity Pathway Analysis (QIAGEN) and Reactome. The transcriptomic data generated in this study have been deposited in the Genome Sequence Archive (GSA) database under accession number PRJCA042290. To determine the impact of COVID-19 infection on human HSPCs, we extracted HSPCs from the scRNA-seq data GSE165080 from Gene Expression Omnibus (GEO) database [17]. This dataset was generated from a cohort of 50 participants, comprising 11 healthy controls (age 43.09 ± 7.57 years; 6 female/5 male), 5 asymptomatic (41.60 ± 18.34 years; 2 female/3 male), 13 with moderate disease (52.77 ± 9.08 years; 9 female/4 male), 10 with severe disease (65.00 ± 9.40 years; 1 female/9 male), and 11 severe-recovery donors (61.55 ± 13.21 years; 8 female/3 male). As described in the original publication [17], to avoid batch effects, all scRNA-seq datasets were generated by the same operators at the same laboratories using standard operation protocols (SOPs) for cell dissociation, library preparation, and sequencing; in the original analysis, data were processed following the Seurat (v4.0.2) workflow, and the first 20 Harmony-integrated principal components were used to construct the weighted shared nearest neighbor network for clustering. In this study, cells annotated as hematopoietic stem/progenitor cells

(HSPCs) in the original study were extracted, and donors were stratified by age into young (20–39 years) and middle-aged (40–60 years) groups, each further divided by disease status into healthy (non-COVID) and COVID-19 groups. For UMAP analysis, raw UMI counts were normalized to counts per million and log2-transformed. Differentially expressed genes were identified by the Wilcoxon rank-sum test with Bonferroni correction, and the top 300 DEGs were used for dimensionality reduction. Principal component analysis (50 components) followed by UMAP (n_neighbors = 15, min_dist = 0.3, euclidean metric) was performed in Python (scikit-learn; umap-learn 0.5.12). HSC aging signature enrichment score was calculated for any particular gene list using a simple counting algorithm based on a previous study [18]. Briefly, the HSC aging signature gene list was obtained from a previous cross-study meta-analysis, in which each gene is assigned a consistency score (Co) representing the number of independent studies reporting its age-associated transcriptional change. For each group, the query gene list was defined as the differentially expressed genes (DEGs) identified in HSPCs of that group. Each gene in the query list was then scored individually: if the gene was present in the HSC aging signature list (consistency score ≥ 1), its consistency score was added; if the gene was not present in the aging signature list, a value of −1 was assigned. The enrichment score was calculated as the sum of these gene-level values divided by the total number of genes in the query list: Enrichment score = (Σ S_k)/N, where S_k = Co_k if gene k is present in the HSC aging signature list and −1 otherwise. GSEA of the RIG-I signaling and ROS signature gene sets was performed on the ranked gene lists of HSPCs from each group. The RIG-I signaling and ROS signature gene sets were obtained from KEGG_RIG_I_LIKE_RECEPTOR_SIGNALING_PATHWAY and GOBP_REACTIVE_OXYGEN_SPECIES_METABOLIC_PROCESS.

LNP-ASO preparation and treatment

ASOs targeting BIRC6 were designed, synthesized, and encapsulated into lipid nanoparticles (LNPs). LNPs were functionalized with anti-mouse CD117 monoclonal antibody (clone 2B8, BioLegend) for HSC-targeted delivery. For *in vivo* treatment, middle-aged infected mice received intravenous injections of LNP-ASO (10 μg per mouse) at 14 and 21 days post-infection. Analyses were performed at indicated time points after treatment.

High-throughput screening

A natural anti-inflammatory product library comprising 465 compounds (MedChem Express) was screened using HSCs isolated from infected middle-aged mice at 28 dpi. Compounds were assessed at 10 μM for their ability to reduce mitochondrial ROS (DCFDA staining) and enhance ATP production (CellTiter-Glo assay). The primary screen was designed as a ranking-based qualitative assay, and no formal multiple-testing procedure was applied at this stage. Hit selection was based on the consistent magnitude of effects across all three replicates, and compounds showing a clear reduction of mitochondrial ROS together with increased ATP production relative to vehicle controls in every replicate were retained as hits. Candidate hits were subsequently confirmed in dose-response validation assays with statistical testing, among which Bilobetin exhibited the most robust and consistent efficacy in both readouts and was selected for *in vivo* evaluation.

Pharmacological treatments

For *in vivo* MitoQ treatment, mice received intraperitoneal injections of MitoQ (500 μM, 100 μL, MedChem Express) on days 14 and 21 post-infection. For Bilobetin treatment, mice received intraperitoneal injections of Bilobetin (1 mg/kg, MedChem Express) on days 14 and 21 post-infection. For cFP treatment, mice received intraperitoneal injections of cFP (10 mg/kg, MedChem Express) on days 14 and 21 post-infection. For *ex vivo* CCCP treatment, HSCs were treated with 15 μM CCCP (MedChem Express) for 24 h to induce mitophagy-mediated clearance of damaged mitochondria.

Cytokines measurement

Cytokines (IL-1α, IL-6, MCP-1, CXCL1) levels in plasma were measured by ELISA Kit (Biorigin) according to the manufacturer's instructions.

HSC differentiation assay

BM HSCs were sorted at 28 dpi. Sorted HSCs were centrifuged at 500 × g for 5 min, resuspended in complete macrophage differentiation medium (DMEM/F12 supplemented with 10% heat-inactivated FBS, 50 ng/mL recombinant murine M-CSF, 100 U/mL penicillin, and 100 μg/mL streptomycin). Differentiated macrophages were stimulated with Poly(I:C) (10 μg/mL) for 6 h, followed by flow cytometric analysis of p16 and IL-6 expression. For Bilobetin treatment in this assay, differentiated macrophages were treated with Bilobetin (2 μM) concurrently with Poly(I:C) stimulation for 6 h.

Subcellular fractionation and extraction of cytosolic mtRNA and mtDNA

Subcellular fractionation and extraction of cytosolic mtRNA and mtDNA were conducted following previous studies [19, 20]. Cells were washed twice with ice-cold PBS and immediately processed. Subcellular fractionation was performed by selective plasma-membrane permeabilization with digitonin (Sigma-Aldrich). Cell pellets were gently resuspended in ice-cold PBS containing 150 μg/mL digitonin and incubated on ice for 10 min with occasional gentle mixing. The samples were centrifuged at 1,000 × g for 5 min at 4 °C to pellet nuclei and intact mitochondria; the supernatant was carefully collected as the cytosolic fraction. When residual membrane debris was visible, the cytosolic supernatant was further clarified by centrifugation at 10,000 × g for 10 min at 4 °C. For cytosolic mtRNA, RNA was extracted from the cytosolic fraction using the RNeasy Micro Kit (QIAGEN) according to the manufacturer's instructions, including an on-column DNase I digestion step to eliminate residual genomic DNA contamination. RNA concentration and purity were determined spectrophotometrically (NanoDrop ND-1000). First-strand cDNA was synthesized using the High-Capacity cDNA Reverse Transcription Kit (Thermo Fisher Scientific) with random hexamers according to the manufacturer's instructions. To distinguish mtRNA from contaminating mtDNA, parallel cytosolic RNA aliquots were treated with RNase A (Thermo Fisher Scientific) before reverse transcription; sensitivity of the mitochondrial-encoded transcript signal to RNase A digestion confirmed its RNA origin. For cytosolic mtDNA, DNA was extracted from an equivalent cytosolic aliquot using the DNeasy Blood & Tissue Kit (QIAGEN) or QIAamp DNA Micro Kit (QIAGEN) according to the manufacturer's instructions. DNA concentration was measured with a NanoDrop spectrophotometer, and samples were stored at −20 °C until analysis.

Quantitative RT-PCR (qRT-PCR)

RNA was extracted from cells using a RNeasy® Micro Kit (QIAGEN, Hilden, Germany) and was reverse-transcribed into cDNA using a PrimeScript™ RT reagent Kit (TaKaRa, Shiga, Japan) according to the manufacturer's instructions. The mRNA expression levels of indicated genes were measured by a CFX96™ Real-Time system (BioRad, Hercules, CA, USA) with a GoTaq® qPCR Master Mix (Promega, Madison, WI, USA). Relative expression was calculated using the $2^{-\Delta\Delta Ct}$ method, with *Hprt* as the normalization control and the Y-Uninfected group as the reference group. The primers were listed in Supplementary Table 2.

Histopathological analysis

Lung tissues were randomly sampled from each mouse, fixed in 4% (v/v) formalin for 24 h, and routinely processed into paraffin-embedded tissue blocks. Tissue sections were stained with hematoxylin and eosin (H&E) and examined under a light microscope (Olympus BX53, Japan). To account for the heterogeneous distribution of pulmonary lesions, at least two sections were prepared from different levels of each lung sample, and four non-overlapping microscopic fields were randomly selected from each section for evaluation. Histopathological scoring was performed under blinded conditions: all slides were coded by an investigator who did not participate in the evaluation, and the coded slides were scored by two investigators who were unaware of the group allocation. For each field, the severity of histopathological changes, including pulmonary inflammation, interstitial pneumonia, edema, alveolitis, bronchiolitis, alveolar destruction, mononuclear cell infiltration, pulmonary hemorrhage, and peribronchiolar inflammation, was graded semi-quantitatively on a 5-point scale (0, no pathological changes; 1, mild; 2, moderate; 3, severe; 4, extremely severe). The mean score of all evaluated fields was calculated for each animal and used for the statistical analysis, and the group codes were revealed only after all scoring had been completed.

Statistical analysis

All statistical analyses were performed using GraphPad Prism 9.0 software. Quantitative data are presented as mean ± SD, with the number of independent biological replicates (n) explicitly stated in figure legends. Quantitative data were normalized to the mean of the corresponding control group where indicated. Normality was assessed using the Shapiro-Wilk test, and homogeneity of variance was assessed using the Brown-Forsythe test. Comparisons between two groups used unpaired two-tailed Student's t-tests, while comparisons across three or more groups employed one-way ANOVA with Tukey-Kramer post hoc testing. When the equal-variance assumption was violated, Welch-corrected tests were applied. When data were not normally distributed, non-parametric tests were used, with the Kruskal-Wallis test followed by Dunn's post hoc correction for multi-group comparisons. For sensitivity analyses, central findings were using non-parametric test, as appropriate. $P < 0.05$ was considered statistically significant.

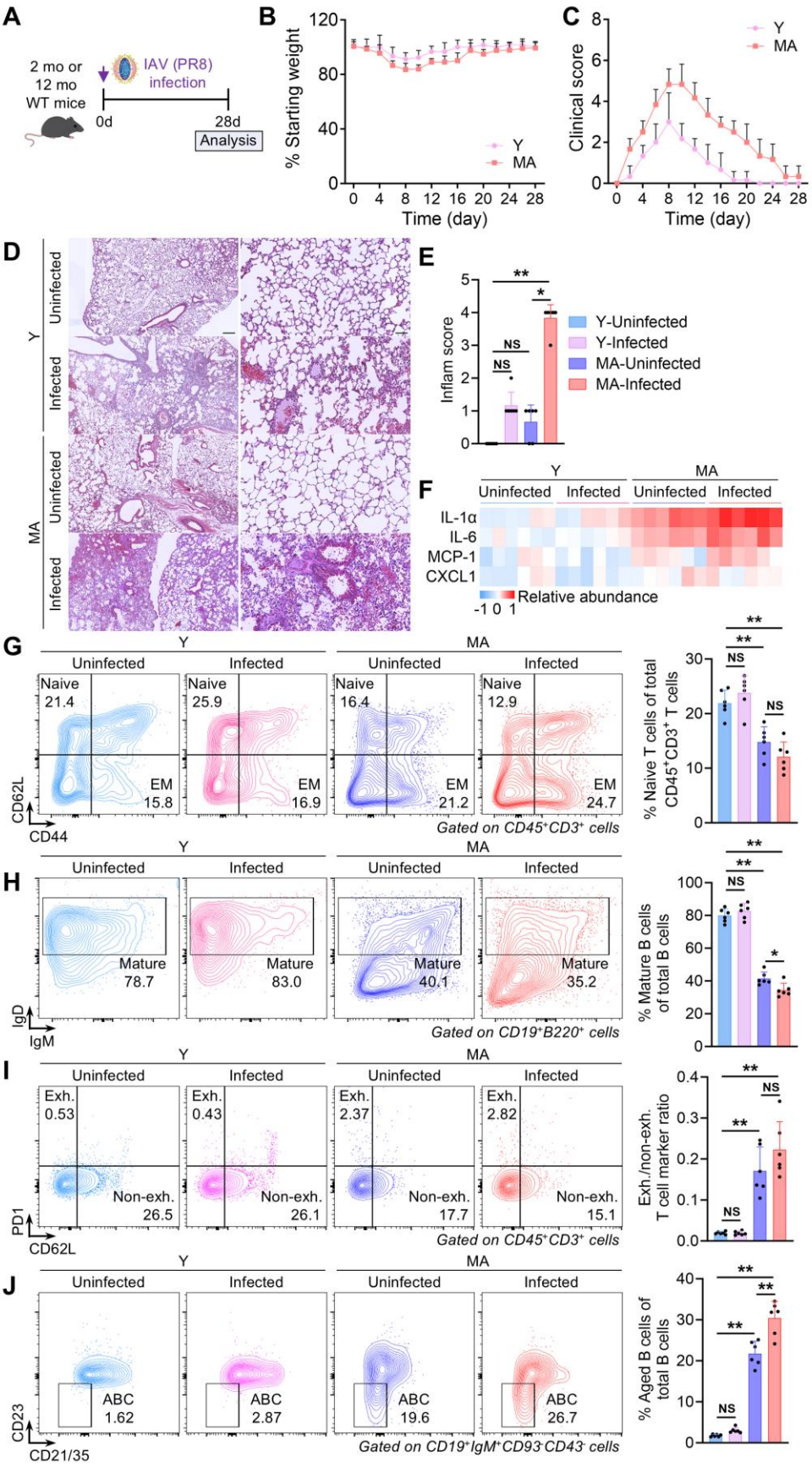

A
2 mo or
12 mo
WT mice
IAV (PR8)
infection
0d
28d
Analysis
B
% Starting weight
Time (day)
Y
MA
C
Clinical score
Time (day)
Y
MA
D
Y
MA
Uninfected
Infected
E
Inflam score
Y-Uninfected
Y-Infected
MA-Uninfected
MA-Infected
NS
F
Y
MA
Uninfected
Infected
IL-1α
IL-6
MCP-1
CXCL1
Relative abundance
G
Naive
21.4
25.9
16.4
12.9
EM
15.8
16.9
21.2
24.7
CD62L
CD44
Gated on CD45+CD3+ cells
% Naive T cells of total CD45+CD3+ T cells
H
Mature
78.7
83.0
40.1
35.2
IgD
IgM
Gated on CD19+B220+ cells
% Mature B cells of total B cells
I
Exh.
0.53
0.43
2.37
2.82
Non-exh.
26.5
26.1
17.7
15.1
PD1
CD62L
Gated on CD45+CD3+ cells
Exh./non-exh. T cell marker ratio
J
ABC
1.62
2.87
19.6
26.7
CD23
CD21/35
Gated on CD19+IgM+CD93-CD43- cells
% Aged B cells of total B cells

Figure 1. **IAV infection accelerates immunosenescence in middle-aged mice. (A)** Experimental schema: young (Y, 2-month-old) and middle-aged (MA, 12-month-old) WT mice were intranasally inoculated with IAV (PR8, 100 PFU) and monitored for up to 28 days post-infection (dpi). **(B)** Body weight changes of Y and MA mice following IAV infection ($n = 6$). **(C)** Clinical scores of Y and MA mice following IAV infection ($n = 6$). **(D)** Representative H&E staining of lung inflammation at 28 dpi ($n = 6$). Scale bars, 100 μm. **(E)** Inflammation scores of Y and MA mice following IAV infection ($n = 6$). **(F)** Plasma SASP factor levels (IL-1α, IL-6, MCP-1, CXCL1) at 28 dpi measured by ELISA ($n = 6$). **(G, H)** Flow cytometric analysis of (G) the percentage of naive T cells ($CD44^-CD62L^+$) within the total $CD45^+CD3^+$ T cell populations, as well as (H) the percentage of mature B cells (IgM^+IgD^+) within the total B cell population ($CD19^+B220^+$) in peripheral blood at 28 dpi ($n = 6$). **(I, J)** Representative flow cytometric analysis of (I) the ratio of T cells with an exhausted phenotype relative to those with a non-exhausted phenotype (percentage of $PD1^+CD62L^-$ cells)/(percentage of $PD1^-CD62L^+$ cells), as well as (J) the percentage of aged B cells ($CD21/CD35^-CD23^-$) of total mature B cells ($CD19^+IgM^+CD93^-CD43^-$) in peripheral blood at 28 dpi ($n = 6$). Data are expressed as mean ± standard deviation (SD), one-way ANOVA with Tukey-Kramer post hoc testing was used for multi-group comparisons unless stated otherwise. Non-parametric alternatives are used for statistical tests and Kruskal-Wallis test with Dunn's post hoc correction for multi-group comparison in (E). $^*P < 0.05$, $^{**}P < 0.01$. IAV, influenza A virus; Y, young; MA, middle-aged; WT, wild-type; PFU, plaque-forming units; dpi, days post-infection; H&E, hematoxylin and eosin; SASP, senescence-associated secretory phenotype; IL-1α, interleukin-1α; IL-6, interleukin-6; MCP-1, monocyte chemoattractant protein-1; CXCL1, C-X-C motif chemokine ligand 1; ABCs, age-associated B cells.

RESULTS

IAV infection accelerates immunosenescence in middle-aged mice

Previous studies, including our own, have established that middle-aged mice exhibit baseline immunosenescence characteristics, including elevated senescence markers and impaired function in peripheral immune cells and hematopoietic stem and progenitor cells (HSPCs) [14, 15, 21]. Compared with young counterparts, both immune cells and HSPCs from middle-aged mice display canonical physiological senescence phenotypes and functional deficits, and these basal aging signatures serve as critical determinants of the adverse long-term outcomes following viral infection in middle-aged individuals [5, 11]. While prior evidence has demonstrated that infection accelerates immunosenescence [3, 4], the underlying impacts of viral challenge on hematopoietic immunity remain largely uncharacterized. To delineate this process, we established a non-lethal influenza A virus (IAV) infection model (100 PFU of the H1N1 influenza virus A/Puerto Rico/8/34 (PR8) strain), which permitted a certain survival rate in both young (2-month-old) and middle-aged (12-month-old) mice (Fig. 1A; Supplementary Fig. 1A).

Following IAV infection, middle-aged mice exhibited more pronounced clinical manifestations than young mice, including greater body weight loss, higher clinical scores, and more severe pulmonary inflammation during the acute phase (Fig. 1B, C and Supplementary Fig. 1B). Although both young and middle-aged mice showed substantial recovery by 28 days post-infection (dpi) in terms of body weight and clinical scores, middle-aged mice displayed persistently elevated pulmonary inflammation during both the early phase (7 dpi; Supplementary Fig. 1B) and the convalescent phase (28 dpi; Fig. 1D, E; Supplementary Fig. 1C), indicating unresolved chronic inflammation. Consistent with this, at 28 dpi, middle-aged infected mice exhibited significantly elevated circulating levels of SASP factors compared with uninfected age-matched controls (Fig. 1F). Moreover, peripheral blood immunophenotyping revealed pronounced immunosenescence in middle-aged infected mice, as evidenced by reductions in naive T cells ($CD44^-CD62L^+$) and mature B cells (IgM^+IgD^+) (Fig. 1G, H), accompanied with an expansion of exhausted T cells ($PD\text{-}1^+CD62L^-$) and age-associated B cells (ABCs; $CD21/CD35^-CD23^-$) (Fig. 1I, J). In contrast, young mice exhibited minimal immunosenescence alterations following IAV infection (Fig. 1F–J). These data collectively demonstrate that IAV infection profoundly accelerates immunosenescence in middle-aged hosts, suggesting that middle age represents a distinct susceptibility window for infection-driven immune aging.

IAV infection induces deep senescence features in middle-aged HSCs

Since immune cell senescence is a defining hallmark of immunosenescence and p16 is well established as a robust biomarker for senescent immune cells [11], we subsequently examined p16 expression across immune compartments. We observed substantially elevated *Cdkn2a* (encoding p16) expression in immune cells from both the spleen and BM of middle-aged mice at 28 days post-IAV infection (Fig. 2A, B). Notably, *Cdkn2a* upregulation was not restricted to the primary infection site (the lung) but was also evident in non-target organs such as the liver (Supplementary Fig. 2A), suggesting a systemic senescence triggered by IAV infection. Within peripheral blood, macrophages exhibited the most pronounced p16 elevation among immune lineages (Fig. 2C), accompanied by their significantly increased IL-6 expression (Supplementary Fig. 2B), consistent with the elevated systemic SASP profile observed. Similarly, lung

tissue macrophages also showed significant p16 and IL-6 elevation, albeit to a lesser extent than circulating macrophages (Supplementary Fig. 2C). Liver macrophages displayed significant but milder senescence and SASP activation compared with lung macrophages (Supplementary Fig. 2D).

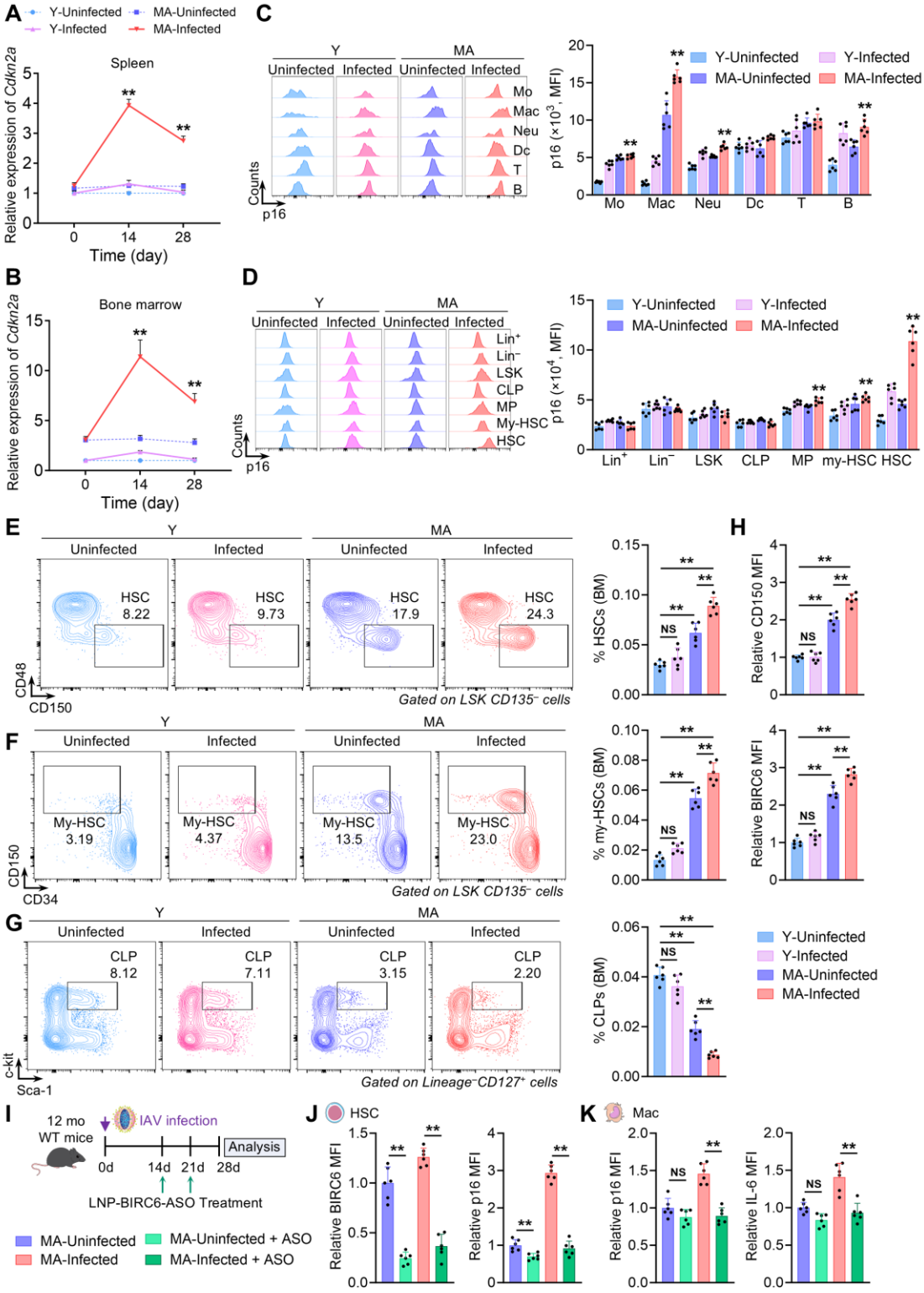


Figure 2. IAV infection induces deep senescence features in middle-aged HSCs. (A, B) qRT-PCR quantification of *Cdkn2a* expression in (A) splenic and (B) bone marrow immune cells from Y and MA mice at 28 dpi (n = 6). **(C)** Flow

cytometric quantification of p16 expression in peripheral blood immune cell subsets (monocytes, macrophages, neutrophils, dendritic cells, T cells and B cells) at 28 dpi (n = 6). **(D)** Flow cytometric quantification of p16 in the BM hematopoietic populations (Lin^+, Lin^-, LSK, MP, CLP, my-HSC, HSC) at 28 dpi (n = 6). **(E)** Representative flow cytometric gating and quantification of frequency of HSC ($Lineage^-Sca\text{-}1^+c\text{-}Kit^+Flt3^-CD150^+CD48^-$) in total live cells in the BM at 28 dpi (n = 6). **(F)** Representative flow cytometric gating and quantification of frequency of my-HSC ($Lineage^-Sca\text{-}1^+c\text{-}Kit^+Flt3^-CD34^-CD150^{high}$) in total live cells in the BM at 28 dpi (n = 6). **(G)** Representative flow cytometric gating and quantification of frequency of CLP ($Lineage^-CD127^+Sca\text{-}1^+c\text{-}Kit^+$) in total live cells in the BM at 28 dpi (n = 6). (H) Flow cytometric quantification of CD150 and BIRC6 expression in HSCs at 28 dpi (n = 6). **(I)** Experimental schema of LNP-BIRC6-ASO treatment. (J) Flow cytometric quantification of BIRC6 and p16 expression in HSCs after LNP-ASO treatment (n = 6). **(K)** Flow cytometric quantification of p16 and IL-6 expression in peripheral macrophages after LNP-ASO treatment (n = 6). All quantitative data are presented as mean ± SD. $^*P < 0.05$, $^{**}P < 0.01$. Comparisons were performed using one-way ANOVA with Tukey-Kramer post hoc testing. qRT-PCR, quantitative real-time PCR.

Given that p16 upregulation was more pronounced in the BM immune cells than in splenic immune cells, we next dissected the senescence landscape at the hematopoietic stem and progenitor cell level. Flow cytometric analysis of the BM hematopoietic hierarchy revealed significant p16 elevation across HSCs, myeloid-biased HSCs (my-HSCs), and multipotent progenitors (MPPs) in infected middle-aged mice. Strikingly, HSCs showed the most robust p16 upregulation, exceeding even that of peripheral macrophages (Fig. 2D). This was accompanied by canonical features of HSC aging, including an expanded HSC pool, increased my-HSC frequency, reduced common lymphoid progenitor (CLP) proportions (Fig. 2E–G; Supplementary Fig. 2E–G), and upregulation of the aging markers CD150 and BIRC6 (Fig. 2H).

To determine whether HSC aging propagates to downstream progeny, we isolated BM HSCs at 28 dpi and differentiated them into macrophages *ex vivo*, followed by Poly(I:C) stimulation to mimic viral sensing. Macrophages derived from infected middle-aged HSCs displayed significantly higher p16 and IL-6 expression upon Poly(I:C) challenge compared with those from uninfected or young counterparts (Supplementary Fig. 2H), demonstrating that infection-induced HSC aging is functionally transmitted to daughter immune cells. Collectively, these findings indicate that HSCs from the BM of infected middle-aged mice exhibit a deep senescence phenotype consistent with previously reported profiles [11].

To determine whether infection-induced immunosenescence could be rescued by targeting aged hematopoietic stem cells (HSCs), we employed a recently established lipid nanoparticle-encapsulated antisense oligonucleotide (LNP-ASO) strategy. This approach selectively suppresses BIRC6 signaling to impair the survival advantages of aged HSCs and thus alleviate immunosenescence [22]. Intriguingly, LNP-BIRC6-ASO treatment during the convalescent phase significantly reduced BIRC6 and p16 expression in HSCs (Fig. 2I, J) and concomitantly decreased p16 and IL-6 expression in peripheral macrophages in infected middle-aged mice (Fig. 2K). These results indicate that deep HSC senescence and its propagation to immune progeny represent actionable targets for therapeutic intervention against IAV infection-triggered immunosenescence.

Persistent MAVS signaling activation in HSCs following IAV infection

To further dissect the molecular mechanisms underlying infection-induced MAVS signaling activation and deep senescence in HSCs, we performed RNA-sequencing (RNA-seq) analysis on BM HSCs isolated from young and middle-aged mice at 28 dpi. Reactome pathway enrichment analysis revealed that the innate immune signaling pathway, particularly the RIG-I/MAVS antiviral signaling axis, was significantly activated in HSCs from infected middle-aged mice. This activation was evident in comparison with both naive young and naive middle-aged control groups (Fig. 3A, B). Flow cytometric validation confirmed that MAVS protein expression and downstream IRF3 phosphorylation (p-IRF3) were significantly elevated in HSCs from infected middle-aged mice (Fig. 3C, D), whereas downstream TBK1 phosphorylation (p-TBK1) showed minimal change (Fig. 3E).

To establish the functional relevance of MAVS signaling in infection-driven HSC aging, we generated *Mx1-Cre*-mediated inducible *Mavs* conditional knockout (KO) mice. MAVS deletion significantly attenuated MAVS signaling (Fig. 3F, G; Supplementary Fig. 3A, B), reduced HSC aging markers (Fig. 3G), and ameliorated downstream immunosenescence phenotypes in infected middle-aged mice (Fig. 3H), positioning MAVS signaling as a necessary node linking IAV infection to HSC aging and immunosenescence. Similarly, pharmacological inhibition of the RIG-I/MAVS axis using the selective inhibitor cyclo(Phe-Pro) (cFP) suppressed downstream IRF3 signaling and alleviated both HSC aging and immunosenescence (Fig. 3I–K). These findings indicate that sustained MAVS signaling activation is a key driver of infection-triggered deep senescence in HSCs.

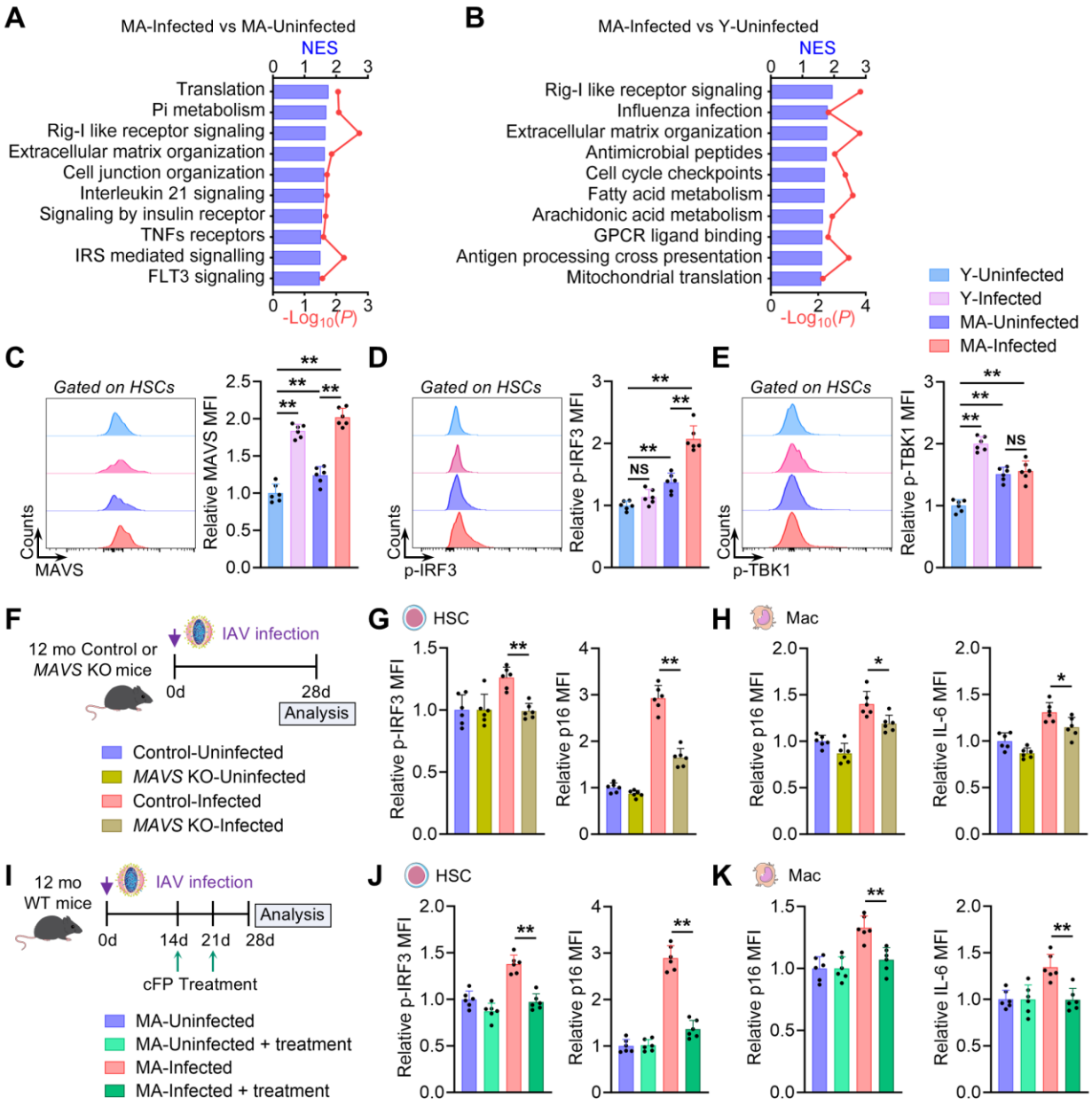


Figure 3. Persistent MAVS signaling activation in HSCs following IAV infection drives immunosenescence. (A) Reactome pathway enrichment analysis of RNA-seq data from BM HSCs of infected vs. uninfected MA mice at 28 dpi. **(B)** Reactome pathway enrichment analysis of RNA-seq data from BM HSCs of infected MA mice vs. uninfected Y mice at 28 dpi. **(C–E)** Flow cytometric quantification of MAVS expression (C), phosphorylation level of IRF3 (D), and TBK1 (E) in HSCs at 28 dpi ($n = 6$). **(F)** Experimental schema of MAVS conditional knockout mice. *Mavs*$^{f/f}$*;Mx1-Cre* mice were administered Poly(I:C) (400 μg per mouse, intraperitoneally, every other day for 7 injections). The control groups received the same Poly(I:C) regimen as the conditional knockout mice, and subsequent experiments were conducted 6 weeks after the first injection. **(G, H)** Flow cytometric quantification of MAVS signaling and immunosenescence markers of HSCs from control and MAVS conditional knockout mice at 28 dpi ($n = 6$). **(I)** Experimental schema of cFP pharmacological treatment. **(J, K)** Flow cytometric quantification of MAVS signaling and immunosenescence after cFP treatment ($n = 6$). Data are expressed as mean ± SD, one-way ANOVA with Tukey-Kramer post hoc testing or two-tailed unpaired Student's t-test was used for comparisons, $^*P < 0.05$, $^{**}P < 0.01$. cFP, cyclo(Phe-Pro); IRF3, interferon regulatory factor 3; MAVS, mitochondrial antiviral signaling protein; RNA-seq, RNA sequencing; TBK1, TANK-binding kinase 1.

Mitochondrial homeostasis imbalance drives sustained MAVS pathway activation

MAVS resides on the mitochondrial outer membrane, with its signaling tightly coupled to mitochondrial homeostasis and HSC fitness [23, 24]. Gene ontology

(GO) enrichment analysis identified marked enrichment of mitochondrial ROS gene signatures in HSCs of infected middle-aged mice (Fig. 4A, B). Flow cytometric analysis confirmed significantly elevated cellular ROS levels (Fig. 4C), increased mitochondrial mass (Fig. 4D), yet paradoxically decreased mitochondrial membrane potential (Fig. 4E) and reduced ATP production (Fig. 4F) in HSCs from infected middle-aged mice. These findings indicate that HSCs from infected middle-aged mice exhibit mitochondrial dysfunction characterized by accumulation of damaged, depolarized mitochondria.

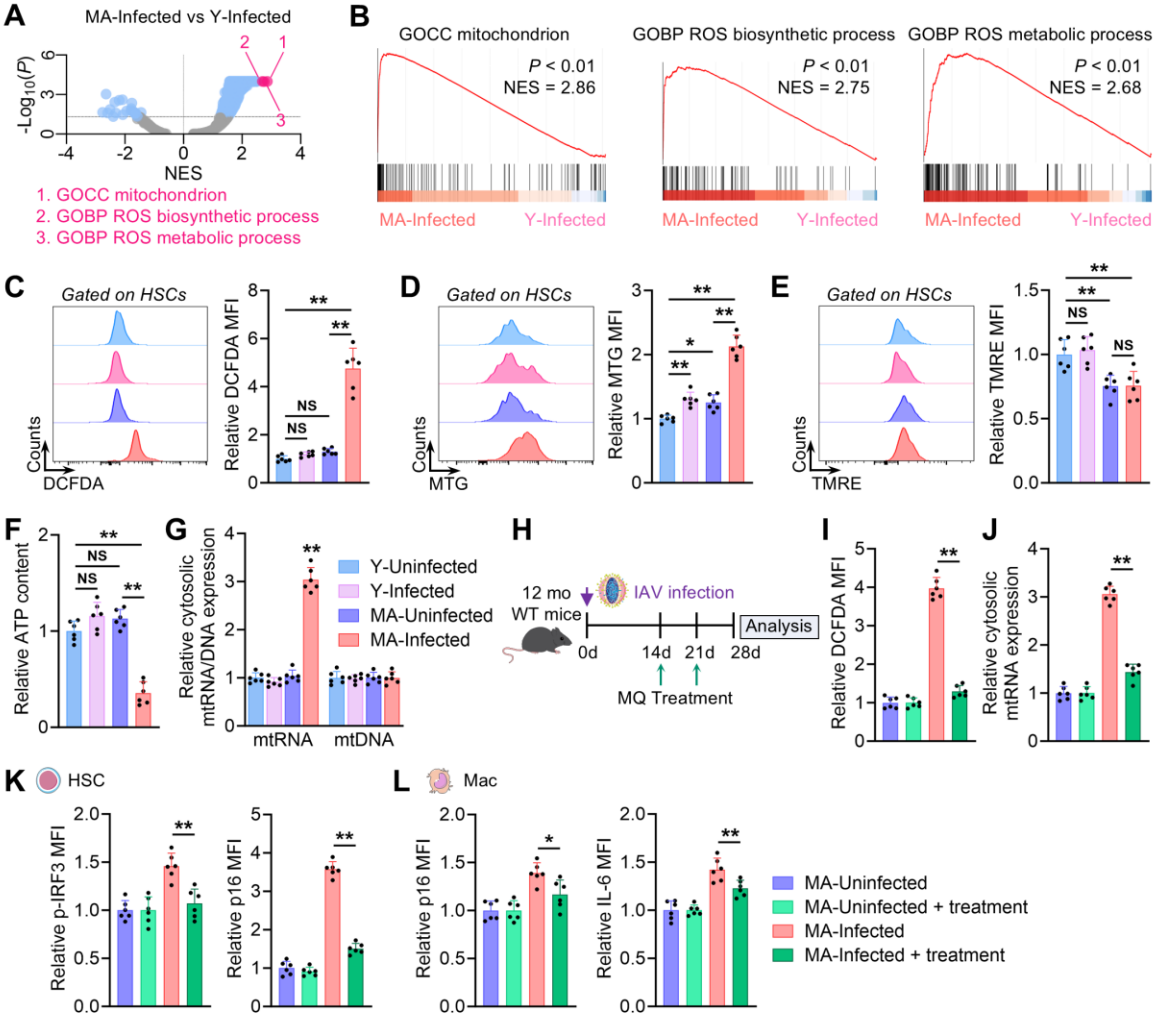


Figure 4. Mitochondrial dysfunction drives sustained MAVS pathway activation and deep senescence in HSCs following IAV infection. (A, B) Gene ontology enrichment analysis and GSEA of RNA-seq data highlighting mitochondrial ROS-related pathways in HSCs from infected MA mice vs infected Y mice. **(C)** Flow cytometric quantification of cellular ROS (DCFDA) in HSCs at 28 dpi (n = 6). **(D)** Flow cytometric quantification of mitochondrial mass (MitoTracker Green, MTG) in HSCs (n = 6). **(E)** Flow cytometric quantification of mitochondrial membrane potential (TMRE) in HSCs (n = 6). **(F)** ATP contents in HSCs measured by CellTiter-Glo assay (n = 6). **(G)** Cytosolic mtRNA and mtDNA levels in HSCs quantified by qRT-PCR (n = 6). **(H)** Experimental schema of MitoQ treatment. **(I–L)** Flow cytometric or qRT-PCR quantification of (I) mitochondrial ROS, **(J)** cytosolic mtRNA levels, (K) MAVS signaling and HSC aging markers, as well as (L) immunosenescence markers after MitoQ treatment (n = 6). Data are expressed as mean ± SD, one-way ANOVA with Tukey-Kramer post hoc testing was used for multi-group comparisons, *P < 0.05, **P < 0.01. ATP, adenosine triphosphate; CCCP, carbonyl cyanide m-chlorophenyl hydrazone; DCFDA, 2',7'-dichlorodihydrofluorescein diacetate; MTG, MitoTracker Green; mtRNA, mitochondrial RNA; ROS, reactive oxygen species.

Recent studies have established that accumulation of cytosolic mitochondrial RNA (mtRNA), resulting from aging-associated mitochondrial homeostasis disruption, is a conserved hallmark of cellular senescence and a key driver of SASP and innate immune activation [19, 25]. Consistent with the persistent MAVS signaling observed at late post-infection time points, which implies aberrant cytosolic nucleic acid accumulation, we detected significantly elevated cytosolic mtRNA levels, but not cytosolic mtDNA levels, in HSCs from infected middle-

aged mice (Fig. 4G). These findings suggest that cytosolic mtRNA accumulation in HSCs likely mediates the sustained MAVS activation following IAV infection. *Ex vivo* treatment with high-dose carbonyl cyanide m-chlorophenyl hydrazone (CCCP), a mitochondrial uncoupler that triggers mitophagy-mediated clearance of damaged mitochondria, partially reversed cytosolic mtRNA accumulation (Supplementary Fig. 4A) and suppressed MAVS signaling activation (Supplementary Fig. 4B) in infected middle-aged HSCs, suggesting that mitochondrial dysfunction-driven mtRNA leakage contributes to sustained MAVS pathway activation. To further test this hypothesis *in vivo*, we treated infected middle-aged mice with the mitochondria-targeted antioxidant MitoQ during the convalescent phase (Fig. 4H). MitoQ treatment effectively restored mitochondrial homeostasis, reducing mitochondrial ROS and mtRNA leakage, while simultaneously suppressing MAVS pathway activation and partially ameliorating HSC aging and immunosenescence phenotypes (Fig. 4I–L; Supplementary Fig. 4C). These results suggest that mitochondrial homeostasis disruption drives infection-induced deep HSC senescence through mtRNA leakage-dependent MAVS activation, and that mitochondria-targeted intervention effectively breaks this pathogenic feedforward loop.

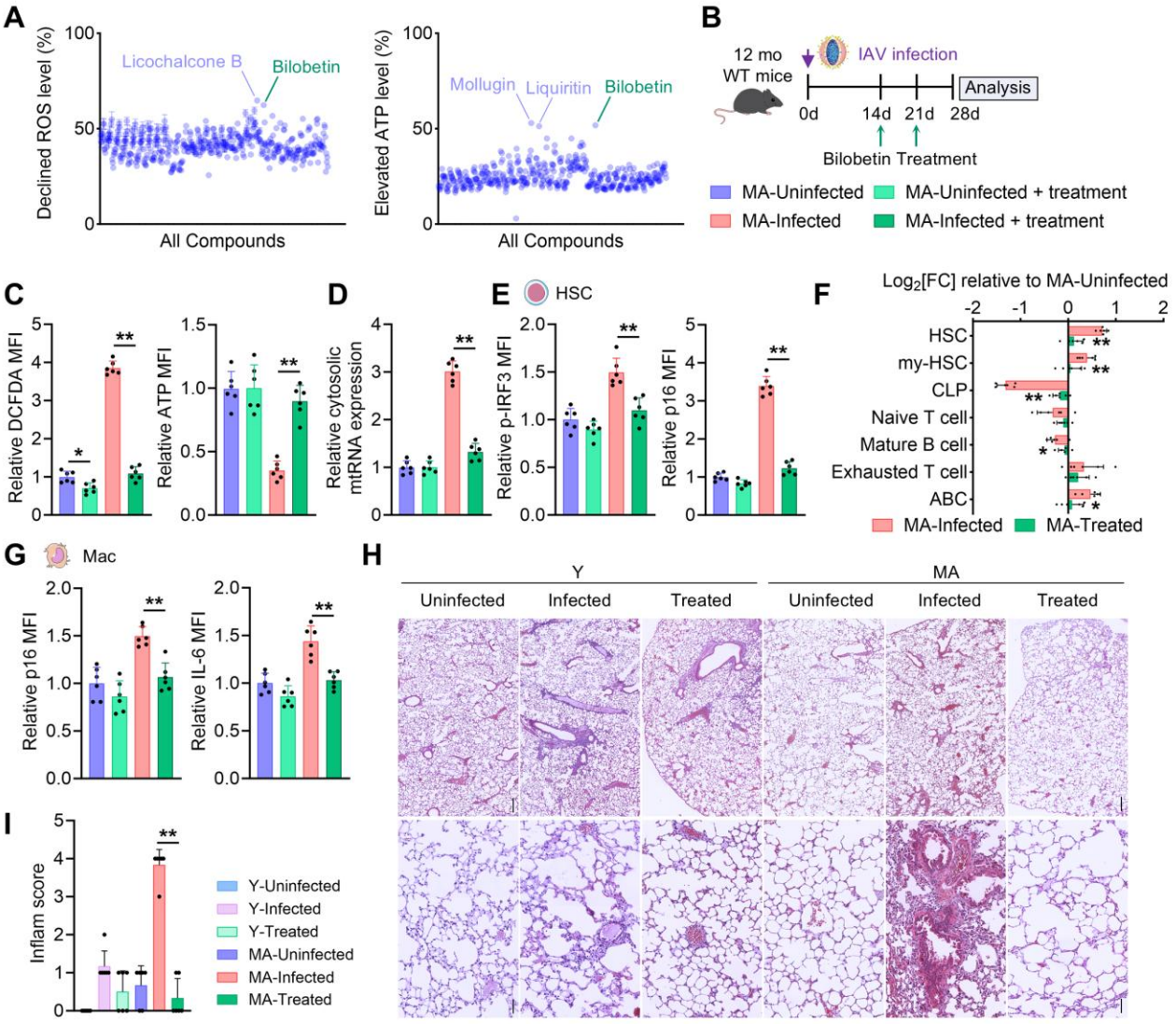


Figure 5. High-throughput screening identifies Bilobetin as a potent mitochondrial-targeting anti-immunosenescence compound. (A) High-throughput screening results: mitochondrial ROS reduction (DCFDA) and ATP production enhancement in HSCs from infected MA mice treated with individual natural compounds (n = 3). **(B)** Experimental schema. **(C–G)** Quantification of (C) mitochondrial ROS and ATP production, (D) cytosolic mtRNA levels, (E) MAVS signaling and HSC aging markers, (F) fold changes of HSPCs and immune cells and (G) immunosenescence markers in infected MA mice following Bilobetin treatment. In (F): fold changes are calculated based on frequencies and MA-Uninfected mice were used as the reference group; HSCs, my-HSCs, and CLPs

are calculated relative to total live cells; naive T cells and T cells with an exhausted phenotype are calculated relative to total $CD45^+CD3^+$ T cells; mature B cells are calculated relative to total $CD19^+$ $B220^+$B cells; aged B cells are calculated relative to total $CD19^+IgM^+CD93^-CD43^-$ mature B cells; and HSC and progenitor populations are from BM, while T and B subpopulations are from PB (n = 6). **(H, I)** Representative H&E staining and quantification of lung inflammation at 28 dpi after Bilobetin treatment (n = 6). Scale bars, 100 μm. Data are expressed as mean ± SD, one-way ANOVA with Tukey-Kramer post hoc testing was used for multi-group comparisons unless stated otherwise. Non-parametric alternatives are used for statistical tests, and Kruskal-Wallis test with Dunn's post hoc correction for multi-group comparison in (I). *$P < 0.05$, **$P < 0.01$.

High-throughput screening identifies Bilobetin as a potent mitochondrial-targeting anti-immunosenescence compound

To identify potent interventions targeting mitochondrial dysfunction-driven HSC aging, we performed an *in vitro* high-throughput screening of a natural anti-inflammatory compound library. Screening was based on two functional readouts in HSCs isolated from infected middle-aged mice: reduced mitochondrial ROS levels and improved mitochondrial metabolic capacity (ATP production). Among all candidate compounds, Bilobetin, a natural biflavonoid derived from *Ginkgo biloba*, exhibited the most robust efficacy in simultaneously mitigating mitochondrial ROS overproduction and augmenting ATP generation (Fig. 5A, B). Other hit compounds, including licochalcone B, mollugin, and liquiritin, showed inferior activity in one or both functional assays.

In vivo dose optimization revealed that relatively low-dose Bilobetin administration effectively reduced mitochondrial ROS and p16 levels in HSCs from infected middle-aged mice, whereas higher doses paradoxically exacerbated these phenotypes (Supplementary Fig. 5A). We therefore evaluated whether short-term intervention could effectively reverse infection-induced deep HSC senescence and immunosenescence, according to strategies reported in recent studies [26, 27]. Indeed, Bilobetin treatment effectively restored mitochondrial function, suppressed MAVS signaling activation, and partially reversed HSC aging in infected middle-aged mice (Fig. 5C–F; Supplementary Fig. 5B). Consistent with the rescue of upstream HSC aging phenotypes, Bilobetin treatment also partially ameliorated peripheral immunosenescence phenotypes in infected middle-aged mice (Fig. 5F, G; Supplementary Fig. 5C, D). Additionally, *ex vivo* treatment with Bilobetin reduced p16 and IL-6 expression upon Poly(I:C) challenge of macrophages derived from infected middle-aged HSCs, suggesting a direct effect of Bilobetin on HSC-derived macrophages (Supplementary Fig. 5D). Bilobetin also significantly ameliorated the persistent pulmonary inflammation observed at the convalescent stage (Fig. 5H, I). Furthermore, Bilobetin administration partially reduced baseline immunosenescence markers in uninfected middle-aged mice (Supplementary Fig. 5A), suggesting broader anti-aging potential beyond infection-induced pathology. These results identify Bilobetin as a novel lead compound for mitochondria-targeted intervention in infection-driven and physiological immune aging.

DISCUSSION

In this study, we characterize the age-dependent landscape of infection-driven HSC aging and immunosenescence using a non-lethal IAV infection model. We find that middle age represents a distinct susceptibility window for infection-induced immune deterioration: young mice exhibit negligible senescent phenotypes and rapidly restore immune homeostasis post-infection, whereas middle-aged mice develop sustained chronic inflammation and accelerated systemic immunosenescence superimposed on baseline physiological aging. Critically, we identify infection-induced deep HSC senescence as a major contributor to systemic immunosenescence, which is associated with sustained immune dysfunction within the observation window of 28 dpi (Fig. 6). This age-dependent divergence aligns with clinical observations of protracted immune impairment in aged adults recovering from severe viral infections [2, 5], supporting the translational relevance of our findings. An important caveat is that the functional consequence of infection-induced HSC senescence is likely context- and time-dependent. During the acute phase of infection, transient senescence and cell-cycle arrest may serve as a protective mechanism, limiting direct viral damage to stem cells and preventing clonal exhaustion under acute stress. This interpretation is consistent with recent evidence that p16-high immune cells promote disease tolerance and extend health span [6]. In contrast, during the chronic phase examined in this study, persistent HSC senescence becomes predominantly detrimental. It drives SASP-mediated chronic inflammation, increased frequency of myeloid-biased HSCs, reduced lymphoid output, and immunosenescence that persists beyond viral clearance within the observation interval (up to 28 dpi).

A key conceptual advance of this work is the proposed hematopoietic-immune senescence stratification model, which resolves two senescence states with qualitatively distinct biological features and therapeutic implications. Peripheral immune cells undergo partial senescence predominantly characterized by SASP-driven inflammation, while BM HSCs enter a deep senescence state defined by concurrent p16

upregulation, increased my-HSC frequency, and mitochondrial dysfunction. Notably, deep-senescent HSCs exhibit upregulation of the anti-apoptotic factor BIRC6, which may confer resistance to conventional senolytic agents and underscores the need for mechanism-guided, cell-type-specific intervention strategies against HSC aging [28]. However, the observation that BIRC6 expression is unchanged in MAVS-deficient and MAVS-signaling-intervened HSCs suggests that these pathways act in parallel rather than in a simple linear hierarchy. Otherwise, a prior study reports enhanced acute IAV resistance in aged (16–19 month-old) mice [29], which appears inconsistent with our findings. Indeed, our findings and previous reports point to a non-monotonic age-effect model: 1) young mice are intrinsically resistant; 2) middle-aged mice occupy a distinct window of susceptibility in which infection superimposed on physiological aging drives pathological immunosenescence; and 3) aged mice, which may already exhibit deep basal senescence, develop only marginal additional pathology upon acute infection. Therefore, the pathological immunosenescence observed in middle-aged mice does not simply scale with the graded physiological aging seen across middle-aged and aged mice [29-31]. The apparently divergent outcomes across studies are therefore most plausibly attributable to differences in age cohort, viral strain and dose, and the timing and endpoints of analysis, underscoring the age-dependent heterogeneity of infection-induced immunosenescence and reinforcing the susceptibility-window concept. While our data support an upstream contribution of deep-senescent HSCs to systemic immunosenescence, HSC ablation and transplantation assays were not performed here, leaving the long-term repopulating, self-renewal, and functional differentiation capacities of deep-senescent HSCs uncharacterized. Further senescent-cell ablation or transplantation assays are required to determine whether deep-senescent HSCs retain a survival advantage, long-term repopulation or self-renewal capacity.

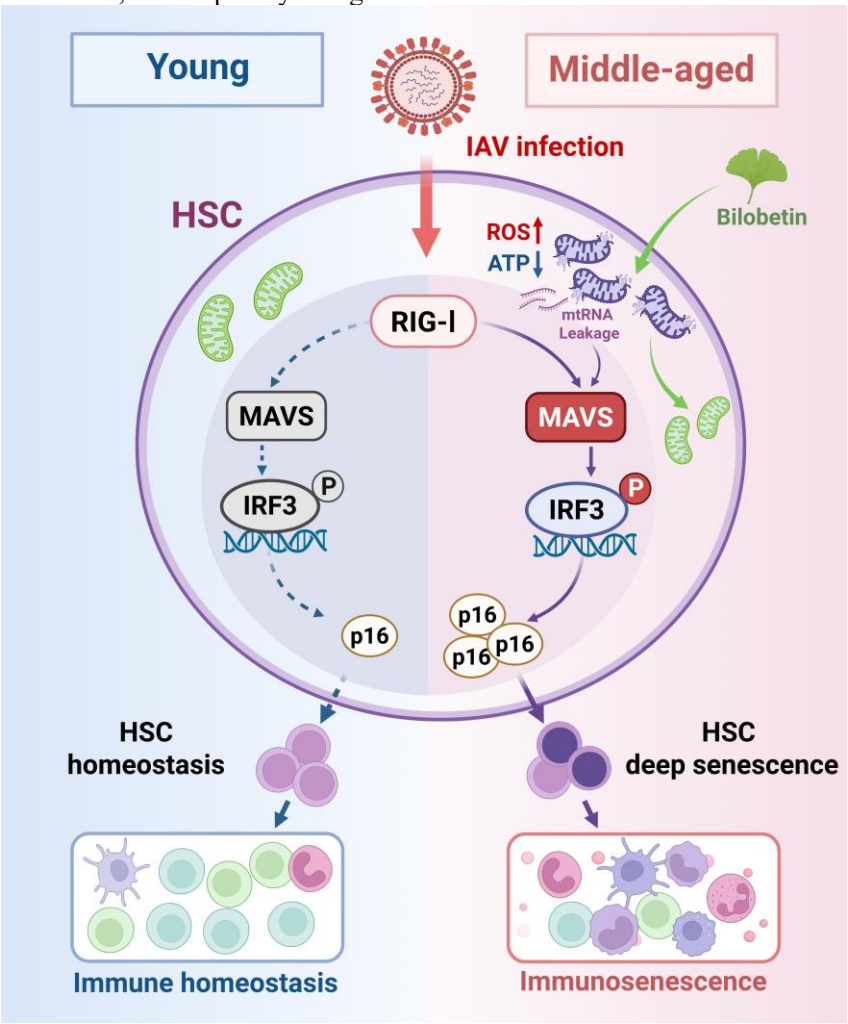


Figure 6. Schematic illustration of how targeting mitochondrial MAVS signaling in deep-senescent HSCs ameliorates infection-driven immunosenescence.

Mechanistically, we identify disrupted mitochondrial homeostasis as a pivotal upstream driver of infection-induced profound HSC senescence. In infected middle-aged mice, HSCs accumulate dysfunctional, depolarized mitochondria, accompanied by elevated cytosolic mtRNA levels and sustained MAVS pathway activation. This mechanism aligns with emerging evidence linking mitochondrial dysfunction and cytosolic double-stranded RNA to cellular senescence and sterile inflammation, positioning MAVS signaling as a shared downstream convergence point that drives pathogenic outcomes under persistent mtRNA stress [19, 25, 32]. Direct causal evidence, however, awaits further investigation, including dynamic time-course analyses of mitochondrial phenotype and function, as well as cytosolic mtRNA levels, in aged HSCs. Whether cytosolic mtRNA accumulation originates from mitochondrial membrane permeabilization (through mPTP-, BAX/BAK-, or other pathways) was not directly examined here and remains mechanistically unresolved. Otherwise, *Mx1-Cre*-mediated deletion is not restricted to HSCs, thus the respective contributions of MAVS in HSCs versus downstream hematopoietic cells (including macrophages) cannot be fully dissociated in this model.

The preliminary cross-strain and cross-virus experiments yielded mixed but directionally consistent results. In the H1N1 influenza A/California/04/2009 (CA04) model, mean p16 and MAVS levels in HSCs were higher in infected than in uninfected middle-aged mice, without reaching statistical significance (Supplementary Fig. 6A–C). In the mouse-adapted SARS-CoV-2 MA10 model, HSC p16 was significantly elevated upon infection, whereas MAVS showed the same upward direction without statistical significance (Supplementary Fig. 6D, E). Infection-associated MAVS elevation was therefore directionally consistent across all three viral models, reaching statistical significance only in the PR8 model. The alterations in the CA04 and MA10 models may reflect differences in disease severity, as indicated by the distinct survival outcomes (Supplementary Fig. 6B, D), and the single observation time point (28 dpi), which may not coincide with the peak of MAVS elevation in these models. Whether infection-induced MAVS elevation is conserved across viral models thus cannot be established from the present data and warrants further validation. Similarly, analysis of human COVID-19 single-cell transcriptomic data revealed that middle-aged COVID-19 patients display heterogeneous HSC transcriptomes and elevated HSC senescence scores compared with age-matched uninfected controls, with concomitant activation of RIG-I and ROS signatures (Supplementary Fig. 6F, G). Nevertheless, these data remain exploratory and supportive, as cell-level comparisons treat multiple cells from the same donor as independent observations, carrying a risk of pseudoreplication. Collectively, these findings suggest that the magnitude of senescence phenotypes and pathway activation may vary with infection severity and viral strain. Future studies with refined characterization schemes for HSC aging and immunosenescence across additional viral infection models, including time-course analyses, will be essential to determine whether mitochondria-targeted interventions have general applicability across post-viral immune sequelae.

Through high-throughput phenotypic screening, we identify Bilobetin, a natural biflavonoid derived from *Ginkgo biloba*, as a potent mitochondria-targeted intervention agent. Bilobetin restores mitochondrial fitness, dampens aberrant MAVS signaling, and ameliorates both HSC aging and downstream systemic immunosenescence. Notably, Bilobetin has pleiotropic activities, including antioxidant effects, improvements in mitochondrial fitness, and inhibition of inflammation and infection [33]. We therefore cannot rule out parallel, MAVS-independent beneficial effects on global mitochondrial fitness or inflammatory signaling, nor direct actions on other tissue compartments. Bilobetin-mediated pulmonary protection may arise, at least in part, from direct modulation of macrophages or other lung-resident cells and thus cannot be specifically attributed to HSC-targeted intervention. Otherwise, the *in vivo* experiments were designed to assess short-term efficacy only, so whether the observed therapeutic benefits persist beyond this period remains to be determined. Future studies are warranted to evaluate long-term safety and durability, analyze phenotype and function of multiple immune cell subpopulations, and explore translational potential of this intervention. In addition, further validation using human primary cells or clinical samples is required to assess the translational potential of these findings.

These findings have important implications for understanding and treating post-viral immune sequelae. The COVID-19 pandemic has highlighted the substantial clinical burden of sustained immune dysfunction in middle-aged survivors of severe viral infections [2, 5]. Our work suggests that virus-induced deep HSC senescence represents a unifying cellular mechanism underlying these post-viral immune syndromes, and that mitochondria-targeted strategies such as Bilobetin offer candidate therapeutic avenues for restoring immune resilience following severe infections. This cellular framework may extend to post-viral syndromes such as long COVID, which commonly present with persistent fatigue, immune exhaustion, and dysregulated hematopoiesis [34]. The mitochondrial MAVS signaling described here may offer a testable cellular hypothesis for

the chronic inflammation and immune dysfunction observed in long COVID patients.

Acknowledgements

We thank He Liu of Army Medical University for technical assistance with animal experiments, and Bin Yu of Tsinghua University for technical assistance with flow cytometry.

Funding

This study was supported by the Beijing Natural Science Foundation (No. 5254049), the National Natural Science Foundation of China (No. 32500654), the Haidian District Science and Technology Association Jinqiao Project, the Young Elite Scientists Sponsorship Program of the Beijing High Innovation Plan (No. 20250993).

Author contributions

Conceptualization: W.L., J.Z. and J.X.. Methodology: W.L., Y.Z., Y.W., R.Z., X.Z., J.Z. and J.X.. Investigation: W.L., Y.Z., Y.W., R.Z., C.X., T.W., M.X., Z.Z., X.Z. and Z.W.. Visualization: W.L., Y.Z. and Y.W.. Funding acquisition: J.Z. and J.X.. Project administration: W.L., J.Z. and J.X.. Supervision: J.Z. and J.X.. Writing—original draft: W.L., J.Z. and J.X.. Writing—review and editing: W.L., X.Z., Z.Z., J.Z. and J.X.. All authors have read and approved the article.

Competing interests

The authors declare no competing interests.

Supplementary Materials

The Supplementary data can be found online at: www.aginganddisease.org/EN/10.14336/AD.2025.0944.

References

[1] Tsuji S, Minami S, Hashimoto R, Konishi Y, Suzuki T, Kondo T, et al. (2022). SARS-CoV-2 infection triggers paracrine senescence and leads to a sustained senescence-associated inflammatory response. Nat Aging, 2:115-124.

[2] Li C, Qian W, Wei X, Narasimhan H, Wu Y, Arish M, et al. (2024). Comparative single-cell analysis reveals IFN-γ as a driver of respiratory sequelae after acute COVID-19. Sci Transl Med, 16:eadn0136.

[3] Lipskaia L, Delval L, Sencio V, Born E, Heumel S, Houssaini A, et al. (2025). Virus-Induced Cellular Senescence Causes Pulmonary Sequelae Post-Influenza Infection. Aging Cell, 24:e70140.

[4] Zeidan RS, Shirali AS, Reinhard S, Picca A, Vial P, Pruinelli L, et al. (2026). Inflammaging: From Mechanisms to Clinical Implications and Targeted Interventions. Aging Dis, online ahead of print.

[5] Jiang Z, Pan W, Chen Y, Zhou D, Ren S, Tong Q, et al. (2025). ApoD mediates age-associated increase in vulnerability to influenza virus infection. Proc Natl Acad Sci U S A, 122:e2423973122.

[6] Triana-Martinez F, Pierantoni A, Graca D, Bergo V, Emelyanov A, Gallerand A, et al. (2026). p16(High) immune cells control disease tolerance as a defense and health span-extending strategy. Immunity, 59:1633-1650.e1639.

[7] de Magalhães JP (2024). Cellular senescence in normal physiology. Science, 384:1300-1301.

[8] Torrance BL, Cadar AN, Panier HA, Martin DE, Lorenzo EC, Jellison ER, et al. (2024). Cellular senescence is a double-edged sword in regulating aged immune responses to influenza. Aging Cell, 23:e14162.

[9] Tian M, Ma J, Li Z, Ye C, Cui X, Wang G, et al. (2025). Senescent cells promote viral infection-associated inflammation and tissue damage through a robust NF-κB pathway. Cell Commun Signal, 23:464.

[10] Zhang X, Zhang Q, Wang L, Li S, Shu HB (2026). Senescent Factors Suppress Innate Antiviral Immunity in Aged Mice via Two Distinct Mechanisms. Aging Cell, 25:e70471.

[11] Doolittle ML, Froemming MN, Rowsey JL, Ruan M, Sapra L, Farr JN, et al. (2026). Aged murine bone marrow myeloid and mesenchymal cells develop unique senescence phenotypes. J Clin Invest, 136.

[12] Yousefzadeh MJ, Flores RR, Zhu Y, Schmiechen ZC, Brooks RW, Trussoni CE, et al. (2021). An aged immune system drives senescence and ageing of solid organs. Nature, 594:100-105.

[13] Andersson R, Mejia-Ramirez E, Florian MC (2025). Haematopoietic ageing in health and lifespan. Nat Cell Biol, 27:1398-1410.

[14] Young KA, Telpoukhovskaia MA, Hofmann J, Mistry JJ, Kokkaliaris KD, Trowbridge JJ (2024). Variation in mesenchymal KITL/SCF and IGF1 expression in middle age underlies steady-state hematopoietic stem cell aging. Blood, 144:378-391.

[15] Liao W, Liu C, Yang K, Chen J, Wu Y, Zhang S, et al. (2023). Aged hematopoietic stem cells entrap regulatory T cells to create a prosurvival microenvironment. Cell Mol Immunol, 20:1216-1231.

[16] Delval L, Creskey M, Valentin C, Bordas C, Raviola S, Lipskaia L, et al. (2026). Senolytic Treatment Reduces Acute and Chronic Lung Inflammation in an Aged Mouse Model of Influenza. Aging Cell, 25:e70480.

[17] Wang X, Bai H, Ma J, Qin H, Zeng Q, Hu F, et al. (2022). Identification of Distinct Immune Cell Subsets Associated with Asymptomatic Infection, Disease Severity, and Viral Persistence in COVID-19 Patients. Front Immunol, 13:812514.

[18] Flohr Svendsen A, Yang D, Kim K, Lazare S, Skinder N, Zwart E, et al. (2021). A comprehensive transcriptome signature of murine hematopoietic stem cell aging. Blood, 138:439-451.

[19] Victorelli S, Eppard M, Martini H, Woo SH, Everts SPA, Lee G, et al. (2025). Mitochondrial RNA cytosolic leakage drives the SASP. Nat Commun, 16:10992.

[20] Victorelli S, Salmonowicz H, Chapman J, Martini H, Vizioli MG, Riley JS, et al. (2023). Apoptotic stress causes mtDNA release during senescence and drives the SASP. Nature, 622:627-636.

[21] Nanishi E, Borriello F, O'Meara TR, McGrath ME, Saito Y, Haupt RE, et al. (2022). An aluminum hydroxide: CpG adjuvant enhances protection elicited by a SARS-CoV-2 receptor binding domain vaccine in aged mice. Sci Transl Med, 14:eabj5305.

[22] Liao W, Shao F, Wang S, Wang Y, Chen X, Zhang Y, et al. (2026). Targeting BIRC6 rejuvenates hematopoietic stem cell aging and immunosenescence. Signal Transduct Target Ther, 11:404.

[23] Yu X, Wang P, Zhou N, Zhang L, Gong X, Guo Q, et al. (2026). Prion-like MAVS fibrils stitch mitochondria to promote a rapid antiviral response. Cell Mol Immunol, 23:204-219.

[24] Chen F, Lu Y, Xu Y, Chen N, Yang L, Zhong X, et al. (2024). Trim47 prevents hematopoietic stem cell exhaustion during stress by regulating MAVS-mediated innate immune pathway. Nat Commun, 15:6787.

[25] Sohn J, Jeon M, Lee H, Lim J, Ham S, Park J, et al. (2026). Phenylalanyl-tRNA synthetase FARS-1/FARSA balances longevity and immunity by downregulating endogenous mitochondrial double-stranded RNAs. Mol Cell, 86:2373-2389.e2313.

[26] Cadar AN, Torrance BL, Fischler SA, Djaba DA, Haddad Z, Teskey DE, et al. (2026). Senolytic Treatment With Dasatinib and Quercetin Reshapes Influenza-Specific CD8 T Cell Responses During Infection in Aged, Vaccinated Mice. Aging Cell, 25:e70345.

[27] Luna A, Chou KN, Wragg KM, Worley MJ, Paruchuri N, Zhou X, et al. (2025). Senolytic treatment attenuates immune cell infiltration without improving IAV outcomes in aged mice. Aging Cell, 24:e14437.

[28] Chang J, Wang Y, Shao L, Laberge RM, Demaria M, Campisi J, et al. (2016). Clearance of senescent cells by ABT263 rejuvenates aged hematopoietic stem cells in mice. Nat Med, 22:78-83.

[29] Lu J, Duan X, Zhao W, Wang J, Wang H, Zhou K, et al. (2018). Aged Mice are More Resistant to Influenza Virus Infection due to Reduced Inflammation and Lung Pathology. Aging Dis, 9:358-373.

[30] Lu J, Li S, Li X, Zhao W, Duan X, Gu X, et al. (2021). Declined miR-181a-5p expression is associated with impaired natural killer cell development and function with aging. Aging Cell, 20:e13353.

[31] Li S, Lu Q, Lu J, Song X, Gu Y, Duan X, et al. (2025). IRF1-RIG-I signaling defects in the aged alveolar epithelial cells may contribute to decreased pulmonary antiviral immune responses. Mech Ageing Dev, 224:112037.

[32] Bergo V, Bousounis P, To Vu G, Douté M, Polyzou A, Lalioti ME, et al. (2026). Lack of MDA5 delays hematopoietic aging by modulating inflammaging and proteostasis in mice. Nat Commun, 17:1645.

[33] Menezes J, Campos VR (2021). Natural biflavonoids as potential therapeutic agents against microbial diseases. Sci Total Environ, 769:145168.

[34] Huang L, Huang T, Liao Y, He S, Hu Y, Lv J, et al. (2024). Long COVID: Current Status, Challenges and Future Directions. iCell, 1:45–56.